The Astrophysical Journal, 987:191 (11pp), 2025 July 10 https://doi.org/10.3847/1538-4357/addc60
© 2025. The Author(s). Published by the American Astronomical Society.
OPEN ACCESS

PKS J0805-0111: A Second Owens Valley Radio Observatory Blazar Showing Highly Significant Sinusoidal Radio Variability—The Tip of the Iceberg

P. V. de la Parra[1], S. Kiehlmann[2], P. Mróz[3], A. C. S. Readhead[4,5], A. Synani[2,5], M. C. Begelman[6,7], R. D. Blandford[8], Y. Ding[9], F. Harrison[9], I. Liodakis[5,10,11], W. Max-Moerbeck[12], V. Pavlidou[2,5], R. Reeves[1], M. Vallisneri[13], M. F. Aller[14], M. J. Graham[15], T. Hovatta[16,17], C. R. Lawrence[13], T. J. W. Lazio[13], A. A. Mahabal[15,18], B. Molina[1], S. O'Neill[19], T. J. Pearson[4], V. Ravi[4], K. Tassis[2,5], and J. A. Zensus[20]
[1] CePIA, Astronomy Department, Universidad de Concepción, Casilla 160-C, Concepción, Chile
[2] Department of Physics and Institute of Theoretical and Computational Physics, University of Crete, 71003 Heraklion, Greece
[3] Astronomical Observatory, University of Warsaw, Al. Ujazdowskie 4, 00-478 Warszawa, Poland
[4] Owens Valley Radio Observatory, California Institute of Technology, Pasadena, CA 91125, USA
[5] Institute of Astrophysics, Foundation for Research and Technology-Hellas, GR-70013 Heraklion, Greece
[6] JILA, University of Colorado and National Institute of Standards and Technology, 440 UCB, Boulder, CO 80309-0440, USA
[7] Department of Astrophysical and Planetary Sciences, University of Colorado, 391 UCB, Boulder, CO 80309-0391, USA
[8] Kavli Institute for Particle Astrophysics and Cosmology, Department of Physics, Stanford University, Stanford, CA 94305, USA
[9] Cahill Center for Astronomy and Astrophysics, California Institute of Technology, Pasadena, CA 91125, USA
[10] NASA Marshall Space Flight Center, Huntsville, AL 35812, USA
[11] Finnish Center for Astronomy with ESO, University of Turku, Vesilinnantie 5, FI-20014, Finland
[12] Departamento de Astronomía, Universidad de Chile, Camino El Observatorio 1515, Las Condes, Santiago, Chile
[13] Jet Propulsion Laboratory, California Institute of Technology, 4800 Oak Grove Drive, Pasadena, CA 91109, USA
[14] Department of Astronomy, University of Michigan, 323 West Hall, 1085 S. University Avenue, Ann Arbor, MI 48109, USA
[15] Division of Physics, Mathematics, and Astronomy, California Institute of Technology, Pasadena, CA 91125, USA
[16] Finnish Centre for Astronomy with ESO (FINCA), University of Turku, FI-20014 Turku, Finland
[17] Aalto University Metsähovi Radio Observatory, Metsähovintie 114, 02540 Kylmälä, Finland
[18] Center for Data Driven Discovery, California Institute of Technology, Pasadena, CA 91125, USA
[19] Department of Physics, Princeton University, Jadwin Hall, Princeton, NJ 08540, USA
[20] Max-Planck-Institut für Radioastronomie, Auf dem Hügel 69, D-53121 Bonn, Germany
Received 2024 August 2; revised 2025 May 5; accepted 2025 May 15; published 2025 July 8

Abstract

Owens Valley Radio Observatory observations of the supermassive black hole binary (SMBHB) candidate PKS 2131−021 revealed, for the first time, six likely characteristics of the phenomenology exhibited by SMBHBs in blazars, of which the most unexpected and critical is sinusoidal flux density variations. We have now identified a second blazar, PKS J0805−0111, showing similar variations, with a period of 1.422 ± 0.005 yr in the rest frame of the $z = 1.388$ object. PKS J0805−0111 displays five of the six characteristics observed in PKS 2131−021. To estimate the significance of the sinusoidal variations, we generate 10^6 simulated light curves that reproduce the radio variability characteristics of PKS J0805−0111 and show that the global probability that the periodicity we detect is due to the red-noise tail of the power spectral density is $p = 6.7 \times 10^{-5}$ (3.82σ). This shows that PKS 2131−021 is not a unique case. The discovery of these two objects in a sample of 1158 blazars allows us to reject, at a p-value $\sim$0.003, the null hypothesis that the sinusoidal variations in these two blazars are all due to a red-noise process. We estimate that the number of SMBHB candidates among blazars is $\sim$1 in 100.

Unified Astronomy Thesaurus concepts: Blazars (164); Relativistic jets (1390)

1. Introduction

Galaxy mergers play a major role in the formation of structure in the Universe and often create active galactic nuclei (AGN; C. J. Conselice 2014), some of which are powered by supermassive black hole binaries (SMBHBs; P. F. Hopkins et al. 2008). The evolution of SMBHBs was first discussed by M. C. Begelman et al. (1980), who pointed out that when the binary becomes sufficiently tightly bound the orbit is shrunk by gravitational radiation until the two SMBHs coalesce. Thus, searches for SMBHBs hold great promise, not only for detailed studies of AGN and relativistic jets, but also for multi-messenger astronomy. The discovery of the stochastic background of gravitational waves (GWs) with periods of months to years (G. Agazie et al. 2023a; EPTA Collaboration et al. 2023), thought to be due to SMBHBs (e.g., G. Agazie et al. 2023b), has provided an additional impetus to this field.

The many channels by which SMBHBs might possibly be observed, and theoretical models of SMBHB systems, have recently been reviewed by D. J. D'Orazio & M. Charisi (2023), and we do not discuss these in this paper, because, as these authors point out, it is not easy to choose between the multiplicity of channels. This field is in its infancy and, like all new astrophysical phenomena, it must be driven by the observations rather than by theory and speculation. These include periodic signals in AGN light curves found by D. J. D'Orazio & M. Charisi (2023), spectroscopic or jet-related signatures indicative of binary motion, and nanohertz gravitational waves from pulsar timing arrays.

We are engaged in a search for statistically significant periodic and quasi-periodic oscillations in flux density among the $\sim$1830 blazars in the Owens Valley Radio Observatory (OVRO) 40 m Telescope 15 GHz monitoring program, of which 1158 form a complete well-defined sample (J. L. Richards et al.

Original content from this work may be used under the terms of the Creative Commons Attribution 4.0 licence. Any further distribution of this work must maintain attribution to the author(s) and the title of the work, journal citation and DOI.

2011). Compelling evidence of a stable periodicity in the blazar PKS 2131−021 from this program was recently presented by S. O'Neill et al. (2022, hereafter O22), who showed that it is highly unlikely to be due to random fluctuations due to the red noise in the variability spectrum. Periodicity in PKS 2131−021, based on the OVRO observations, was first reported by G.-W. Ren et al. (2021a). More recently, S. Kiehlmann et al. (2025) discovered coherent sinusoidal variations in PKS 2131 −021 from 2.7 GHz to optical wavelengths. The very broad-band coherent sinusoidal variations and the stability of the period over 47.9 yr amount to compelling evidence that PKS 2131−021 is an SMBHB.

Based on their observations of PKS 2131−021, O22 drew attention to six likely characteristics of SMBHBs as revealed through their blazar light curves:

1. Strong sinusoidal flux density variations.
2. Long-term stability of the period.
3. Rapid disappearance of the sinusoidal fluctuations in less than one period.
4. Reappearance of sinusoidal fluctuations in less than one period and with different amplitude.
5. The sinusoidal variations are in addition to the regular variations in the blazar; in other words, the mean flux density is elevated during the periods of the sinusoidal variations.
6. Variations in the period of ∼10%, or variations in phase within ∼10% of a cycle.

PKS J0805−0111 exhibits all of these characteristics except #5. G.-W. Ren et al. (2021b) first drew attention to PKS J0805 −0111 as an interesting SMBHB candidate based on our 40 m Telescope monitoring observations. We show that the global p-value of the periodic behavior in PKS J0805−0111 being due to random variations in the red-noise tail is small (p-value $= 6.7 \times 10^{-5}$, 3.82σ), and therefore passes the 3σ threshold we have adopted for a strong SMBHB candidate (O22).

The source PKS J0805−0111 has been identified as a flat-spectrum radio quasar (S. E. Healey et al. 2007), i.e., $\alpha > -0.5$, where $S \propto \nu^{\alpha}$. The spectroscopic redshift of $z = 1.388$ was measured by S. E. Healey et al. (2008).

As discussed by O22, blazars showing evidence of periodicities should not be considered bona fide periodic or quasi-periodic oscillator candidates unless it can be shown that there is a very low global probability (p-value $< 1.3 \times 10^{-3}$, i.e., 3σ) that the periodicity is due to red-noise tail fluctuations. This can be done through a careful analysis of the power spectral density (PSD) with simulations that reproduce both the observed PSD and the observed probability density function (PDF) seen in the light curve.

There are now several SMBHB candidates identified through a variety of methods (for a recent review see D. J. D'Orazio & M. Charisi 2023). Periodic variability has been systematically explored in large-scale optical surveys for AGN (e.g., M. J. Graham et al. 2015; M. Charisi et al. 2016). Apart from PKS 2131−021, the only other strong blazar candidates are PG 1553+113 (γ-rays: M. Ackermann et al. 2015; X-rays: T. Aniello et al. 2024; optical: Y. Chen et al. 2024) and OJ 287 (optical: A. Sillanpaa et al. 1988; M. J. Valtonen et al. 2016; optical and radio: L. Dey et al. 2021).

In the radio band, while claims have been made for quasi-periodicities in several sources, PKS 2131−021 has been, until now, the only blazar showing clear sinusoidal variability, a signal that passes the global (i.e., the *look-elsewhere effect* corrected) 3σ significance threshold (O22).

Therefore, PKS J0805−0111 is only the second blazar to be identified as a high-probability SMBHB showing sinusoidal variations in its radio light curve. This demonstrates that PKS 2131−021 is not a unique, isolated, case. Clearly, while this is an easily identifiable class of AGN, it requires long-term radio monitoring observations in order to capture the 3–5 yr periods of the candidates. In this paper we argue that at least 1 in 1000 blazars shows strong sinusoidal variations over a large fraction of a 15 yr light curve, and they should therefore be considered strong SMBHB candidates. Furthermore, we argue that, taking into account those blazars in which sinusoidal fluctuations are weaker, or absent, for a significant fraction of the time, at least 1 in 100 blazars is an SMBHB candidate.

The radio observations of PKS J0805−0111 are described in Section 2. The analysis identifying PKS J0805−0111 as a strong SMBHB candidate is presented in Section 3. The significance of periodicities discovered in this case and in searches of OVRO radio light curves in general is discussed in Section 4. The effects of the sample size are discussed in Section 5. Infrared and optical observations of PKS J0805 −0111 are described in Section 6. The hard X-ray and γ-ray emission from PKS J0805−0111 is discussed in Section 7. The fact that we are only identifying a small fraction of the blazars that are potential SMBHB candidates is considered in Section 8. The search for evidence of gravitational waves from PKS J0805−0111 is discussed in Section 9. Our conclusions are presented in Section 10.

For consistency with our other papers, we assume the following cosmological parameters: $H_0 = 71$ km s^{-1} Mpc^{-1}, $\Omega_m = 0.27$, and $\Omega_\Lambda = 0.73$ (E. Komatsu et al. 2009). None of the conclusions would be changed were we to adopt the best model of the Planck Collaboration (Planck Collaboration et al. 2020).

2. Radio Observations—OVRO 40 m

The OVRO 40 m telescope has been monitoring ∼1830 blazars at 15 GHz since 2008 (J. L. Richards et al. 2011). The telescope is equipped with a cryogenic pseudo-correlation receiver. The observing cadence is ∼1–2 measurements per week. Occasional gaps exist in the data due to weather conditions or hardware problems. The OVRO 40 m Telescope receiver uses a dual-beam switching procedure to remove atmospheric contributions and background emission, as described by A. C. S. Readhead et al. (1989). At this radio frequency the observations are confusion-limited, due to the double-switching technique, which combines three separate fields, and the resulting flux density uncertainty is ∼3–4 mJy. The data reduction and calibration process used to produce the light curves is described by J. L. Richards et al. (2011).

3. Analysis of the Radio Light Curve of PKS J0805−0111

The OVRO 40 m Telescope 15 GHz light curve of PKS J0805 −0111 is shown in Figure 1. As in the case of PKS 2131−021 (O22), a clear sinusoidal variation dominates the variability for a significant fraction of the period of observation. The blue curve shows the least-squares sine wave fit to the data up to MJD 59041, with an observed period of 1240.7 ± 4.6 days, after which the sinusoidal variations disappear.

Due to weather and hardware problems the observations are not equispaced in time. We require statistically robust estimates of the probabilities of various features in the observed light curve, so we need a light-curve simulation

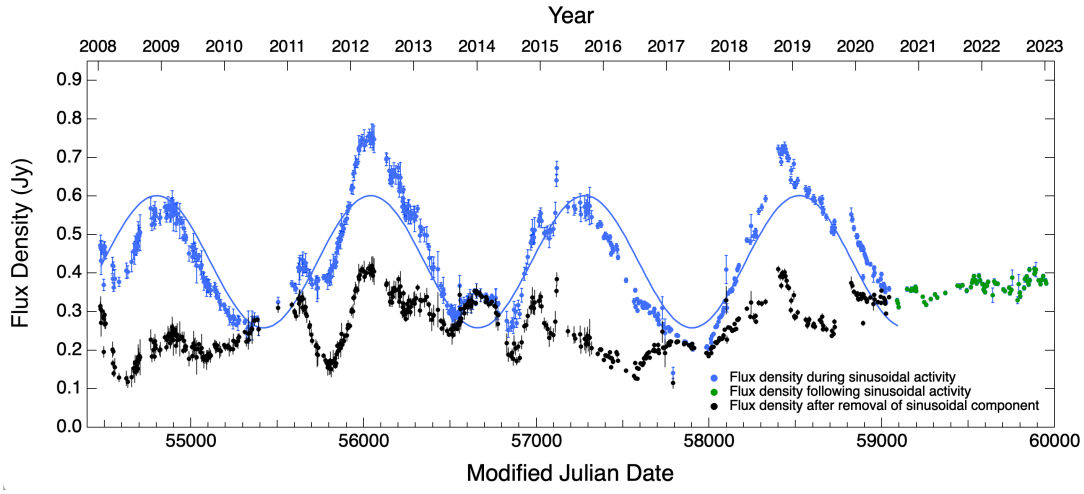

Figure 1. The light curve of PKS J0805−0111. The 15 GHz OVRO data are shown by the blue and green dots. The least-squares sine wave fit to the data up to MJD 59041 is shown by the blue curve, the parameters of which are listed in Table 1. The black dots show the residual randomly varying component of the OVRO light curve after subtracting the sinusoidal component. The periodicity in the light curve up to MJD 59041 has a global significance of 3.82σ, and is not likely to be simply a product of the red-noise tail in the PSD.

procedure that preserves all of the statistical and variation characteristics of the observed light curves, including the identical irregular sampling. We can then simulate a large number of light curves for each blazar and use a Monte Carlo approach to estimate the probability of chance occurrence of various features in the light curve. This approach tests, with the same sampling and observational noise as the real data, the null hypothesis that the observed features in the light curve are a result of red-noise processes. This problem has been considered in a number of papers (W. F. Welsh 1999; P. Uttley et al. 2002; D. Emmanoulopoulos et al. 2010; W. Max-Moerbeck et al. 2014), which simulate light curves with a PSD of the same power-law slope of the variability as that observed in the AGN. Such simulations can be produced with the algorithm introduced by J. Timmer & M. Koenig (1995). However, the underlying PDF of such simulations is Gaussian and does not produce realistic light curves. Radio AGN light curves exhibit "burst"-like events that can often yield long-tailed PDFs. This problem was addressed by D. Emmanoulopoulos et al. (2013) using a simple method to produce light curves that match both the PSD and the PDF of the observed light curves. As desired, the final artificial light curves have the best-matching statistical and variability properties of the observed light curve under the assumption of a red-noise process with a power-law spectrum, and are statistically (and visually) indistinguishable from the true light curves. We are therefore confident that the significances we calculate are robust, having correctly taken into account the red-noise tail in the observed PSD. The details of the simulations are presented in Appendix A.

3.1. Generalized Lomb–Scargle Analysis of the Light Curve

We carried out a generalized Lomb–Scargle (GLS) periodogram analysis (M. Zechmeister & M. Kürster 2009) of the light curve of PKS J0805−0111, from MJD 54476 to MJD 59041, shown by the blue points in Figure 1. This technique is useful for identifying periodicities in unevenly sampled data by least-squares fits of sinusoids to the data. The GLS periodogram is shown in Figure 2. There is only one prominent peak, which is at period $P = 1245$ days and power $\mathcal{P} = 0.77$.

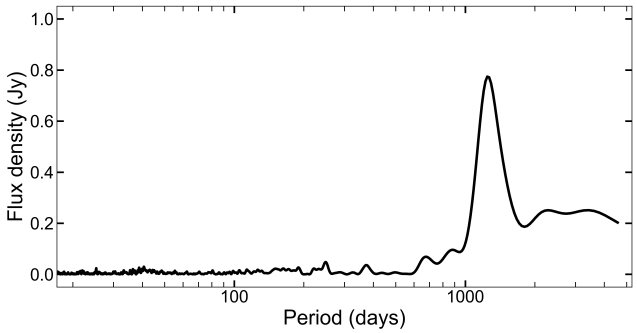

Figure 2. The generalized Lomb–Scargle periodogram of PKS J0805−0111 with power normalized to a range from 0 to 1, where 1 corresponds to a perfect fit, within the uncertainties, to a sine wave.

We use P and $\mathcal{P}$ to distinguish between period and power, respectively.

The frequency span of the periodogram is from $f_{\rm low} = 1/T$, where T is the total observing time, to $f_{\rm high} = N/(2T)$, where N is the total number of measurements. The power was calculated at evenly spaced frequency intervals in steps of $\Delta f = 1/(\zeta T)$. To evaluate the effect of different sampling intervals, we experimented with values of $\zeta = 5$, 10, and 15. No differences were found in the significance analysis, so the value of ζ does not affect our conclusions. To maintain the highest resolution in our analysis we used $\zeta = 15$.

3.2. WWZ Analysis of the Light Curve

The weighted wavelet Z-transform (WWZ) is a Z-transform (J. R. Ragazzini & L. A. Zadeh 1952) that uses wavelet analysis to detect time-dependent periodicities in data. We performed a WWZ analysis of the PKS J0805−0111 light curve, with the results shown in Figure 3. Following the approach presented by G. Foster (1996), we used a time bin of 100 days and tested over periods from 100 to 3500 days. Analysis beyond this range of parameters is not relevant to our conclusions. This analysis clearly shows the presence of a periodic oscillation that dominates, with a period of ∼1250 days from the beginning of the light curve. This periodic signal

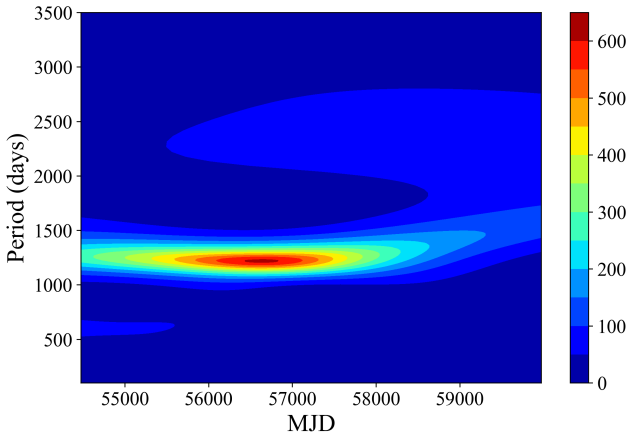

Figure 3. The WWZ analysis of PKS J0805−0111.

remains stable in its period until around MJD 59000, supporting the results obtained from the GLS periodogram.

3.3. Sine-wave Analysis of the Light Curve

We carried out a sine-wave least-squares fitting of the 15 GHz light curve of PKS J0805−0111 following the procedure described by O22, with the result that the period of the sinusoidal variation in PKS J0805−0111 is $P = 1240.7 \pm 4.6$ days, corresponding to a period in the rest frame of the blazar of $P = 519.6 \pm 1.9$ days, at the redshift of 1.388 (S. E. Healey et al. 2008). Results of the fit to the data from MJD 54476 to MJD 59041, when the sinusoidal variations disappeared, are presented in the second column of Table 1.

The best-fit parameters were found by maximizing the following log-likelihood function:

$$\ln \mathcal{L} = -\frac{1}{2}\sum_{i=1}^{N}\left[\frac{(S_i - A\sin(\phi_i - \phi_0) - S_0)^2}{\sigma_i^2 + \sigma_0^2} + \ln(\sigma_i^2 + \sigma_0^2)\right], \quad (1)$$

where $\phi_i = 2\pi(t_i - t_0)/P$, and we adopted $t_0 = 57{,}000$. The parameters (A, ϕ_0, S_0) represent the amplitude of the sine wave, its phase, and the mean flux density, respectively, while σ_0 quantifies the noise in the data.

The uncertainties in the solution that we derive are estimated using the EMCEE sampler (D. Foreman-Mackey et al. 2013) and represent the 68% confidence intervals of the marginalized posterior distribution. However, this analysis does not take the correlated noise into account. The analysis of the correlated noise requires an extensive study of the correlated noise in both the SMBHB candidates and the non-SMBHB objects in the OVRO blazar monitoring sample, which is beyond the scope of this paper.

3.3.1. Analysis of Two Halves of the Light Curve

We have also carried out a sine-wave fitting analysis of the first versus the second half of the light curve of PKS J0805−0111 during the period when the sinusoidal variation is present. The fits are shown in Figure 4. The periods of the two halves agree within the errors (1.3%), but, as can be seen in Figure 4, the phases differ significantly, by ∼12% of the period. This makes an interesting contrast to the situation in which we fitted the two different halves of the OVRO 15 GHz light curve of PKS 2131−021 (O22), in which we found that the *periods* differed by ∼10%. Perusal of the sine-wave-subtracted light curve shown by the black points in Figure 1 reveals that the long-term variations of the blazar needed to produce such an apparent phase shift are typical of the stochastic variations observed in many blazars (see, e.g., W. J. Medd et al. 1972).

In Figure 5(a) we show the light curves from the four cycles folded with a period of 1240.7 days, and in Figure 5(b) we show the same light curves, normalized to the same amplitude and the same offset from zero.

4. Significance of the Periodicity

To calculate the statistical significance of the observed periodicity in PKS J0805−0111 discussed in Section 3, we followed the procedure outlined by O22. It involves counting all simulations for which the p-value of the strongest peak is less than or equal to the p-value of the observed periodicity, the latter being the *local* p-value, which is also estimated from the simulations. A summary of the procedure is given in Appendix A. In our analysis, we found that the period of ∼1245 days has a global significance of 3.82σ (p-value $= 6.7 \times 10^{-5}$), when compared with 1,000,000 simulated light curves, with the best-matching PSD and PDF to PKS J0805−0111. The GLS peak power and period of each of these 1,000,000 simulations are shown in Figure 6. The result of the GLS analysis is shown in Table 2.

Our result (p-value $= 6.7 \times 10^{-5}$) has much lower significance than that claimed by G.-W. Ren et al. (2021b), who estimate a false-alarm probability of 5.75×10^{-8}. Their method is based on that of A. Ciaramella et al. (2004), and assumes that the data are *independent* random Gaussian values, which have a white noise PSD, whereas our blazars have steep power-law PSDs. So this approach is not applicable in the case of PKS J0805−0111.

5. The Effect of Sample Size

A statistically complete, well-defined sample of 1158 blazars was tabulated by J. L. Richards et al. (2011) and was the initial sample in the OVRO monitoring program. This complete sample was selected from the Candidate Gamma-Ray Blazar Survey (CGRaBS; S. E. Healey et al. 2008). The total CGRaBS sample consists of 1625 blazars distributed across the $|b| > 10°$ sky, with flux densities >65 mJy at 4.85 GHz, a radio spectral index $\alpha > -0.5$, and X-ray properties similar to those of blazars detected by the Energetic Gamma Ray Experiment Telescope. The original OVRO 40 m Telescope monitoring sample included only the CGRaBS sources, numbering 1158, above decl. $\delta > -20°$. Since then, many other objects have been added to the 40 m Telescope monitoring program and the whole sample now numbers ∼1830. These additional objects do not comprise a well-defined sample, so we use only the initial sample of 1158 objects in our discussion below. This sample has the advantage that it was selected before the OVRO monitoring observations began, and so has not been influenced in any way by the results.

The global p-value that we derive for PKS J0805−0111 ($p = 6.7 \times 10^{-5}$) is the probability that a red-noise process

Table 1
Results of the Sine-wave Least-squares Fits

Parameter	54476 < MJD < 59041 (full data)	54476 < MJD < 56758 (first two cycles)	56763 < MJD < 59041 (last two cycles)
P (days)	1240.7 ± 4.6	1304.8 ± 15.7	1326.4 ± 10.5
ϕ_0	−0.141 ± 0.025	0.269 ± 0.082	−0.525 ± 0.043
A (Jy)	0.1709 ± 0.0045	0.1657 ± 0.0059	0.2000 ± 0.0058
S_0 (Jy)	0.4295 ± 0.0031	0.4255 ± 0.0041	0.4176 ± 0.0040
σ_0 (Jy)	0.0663 ± 0.0022	0.0646 ± 0.0029	0.0544 ± 0.0028

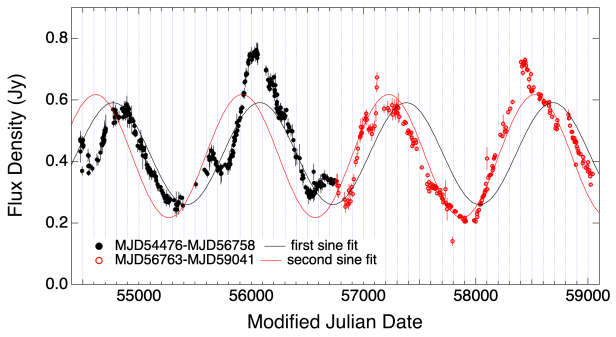

Figure 4. Sine-wave fits to the first and second halves of the light curve of PKS J0805−0111 during the period showing sinusoidal fluctuations. The periods in the two halves are 1304.8 ± 15.7 days (black points and black curve) and 1326.4 ± 10.5 days (red points and red curve).

with the power-law PSD and PDF that best match the light curve of PKS J0805−0111 produces a spurious GLS peak at any tested frequency that is locally at least as significant as the GLS peak detected in PKS J0805−0111.

Under the null hypothesis that the variations in all of the 1158 sources in our sample are random, the p-values will be uniformly distributed between 0 and 1.

The probability, p_1, of obtaining at least one source in the sample with global p-value equal to or less than that found for PKS J0805−0111 ($p = 6.7 \times 10^{-5}$) is

$$p_1 = \sum_{k=1}^{n} \binom{n}{k} p^k (1-p)^{n-k} = 0.075. \quad (2)$$

S. Kiehlmann et al. (2025) showed that the global p-value of the GLS test in PKS 2131−021 is $p = 5.3 \times 10^{-5}$. We can combine the global GLS results for PKS J0805−0111 and PKS 2131−021 to find the probability, p_2, of getting at least two sources with a p-value less than the greater of these two p-values (i.e., $p = 6.7 \times 10^{-5}$):

$$p_2 = \sum_{k=2}^{n} \binom{n}{k} p^k (1-p)^{n-k} = 0.003. \quad (3)$$

Thus the detection of these two sinusoidally varying sources with global p-values both $\leqslant 6.7 \times 10^{-5}$ is significant at the 3×10^{-3} level.

6. Observations of PKS J0805−0111 at Infrared and Optical Energies

The archival optical and infrared light curves of PKS J0805−0111 are shown in Figure 7, which includes 60 V-band data points from the Catalina Real-time Transient Survey (CRTS; A. J. Drake et al. 2009) taken with the 0.7 m Catalina Schmidt Telescope located on Mt. Bigelow, Arizona; and 33 g-band data points from the Zwicky Transient Facility (ZTF; M. J. Graham et al. 2019; F. J. Masci et al. 2019) at the Palomar 48 inch Oschin Schmidt telescope. The CRTS data were collected between 2005 May and 2015 December and the ZTF data between 2018 March and 2023 March. Data were also extracted for the blazar from the Wide Field Infrared Survey Explorer (WISE) covering the 2.8–3.8 μm (W1) and 4.1–5.2 μm (W2) bands over the timeframe from 2010 April to 2022 October. The data are rebinned to a daily cadence using a weighted mean, as is common practice in AGN variability studies.

We have carried out a detailed cross-correlation analysis of the optical and infrared light curves with the OVRO 15 GHz light curve of PKS J0805−0111, identical to that on PKS 2131−021 described by O22, and we find no correlations above the 2σ threshold, so there is no evidence of significant correlations. However, it should be borne in mind that the optical and infrared data are sparse, so that this does not definitively rule out the possibility that there may be a correlation.

7. Observations of PKS J0805−0111 at X-Ray and γ-Ray Energies

Hard X-ray emission from blazars is important, because it is directly connected to the central engine, while soft X-rays from blazars are widely attributed to synchrotron emission (Y. Wang et al. 2024). The hard X-ray emission is attributed to the upscattering of the soft photons of the synchrotron emission (A. Mastichiadis & J. G. Kirk 2002) or to relatively cool structures such as the accretion disk and the broad-line region (C. D. Dermer & R. Schlickeiser 1993; M. Sikora 1994). While periodic oscillations are common in stellar-mass black hole X-ray binary systems, such features are surprisingly rare in AGN X-ray observations (A. C. Gupta et al. 2018). It is only very recently that such periodic signals have come to be widely reported and studied systematically (G. Miniutti et al. 2019; R. Arcodia et al. 2021). In most cases, they originate from stellar-mass compact objects interacting with the AGN accretion disk (A. Franchini et al. 2023). In the particular case of blazars, the X-ray light curves are usually chaotic and aperiodic. X-ray spectral-timing studies have revealed the existence of time-dependent flux and spectral state patterns. G. Bhatta et al. (2018) explored the connections between blazar X-ray variability and other properties such as the spectral hardness and intrinsic X-ray flux in the NuSTAR band. All 13 sources in their sample display high-amplitude, rapid, aperiodic variability with a timescale of a few hours.

PKS J0805−011 has never been the main target of modern X-ray telescopes like Chandra and XMM-Newton. There are several Swift/XRT observations but in many cases the off-axis angle is large such that the data are not very useful. We analyzed all Swift/XRT data with off-axis angle smaller than 5′. The stacked spectrum reaches a total net exposure time of

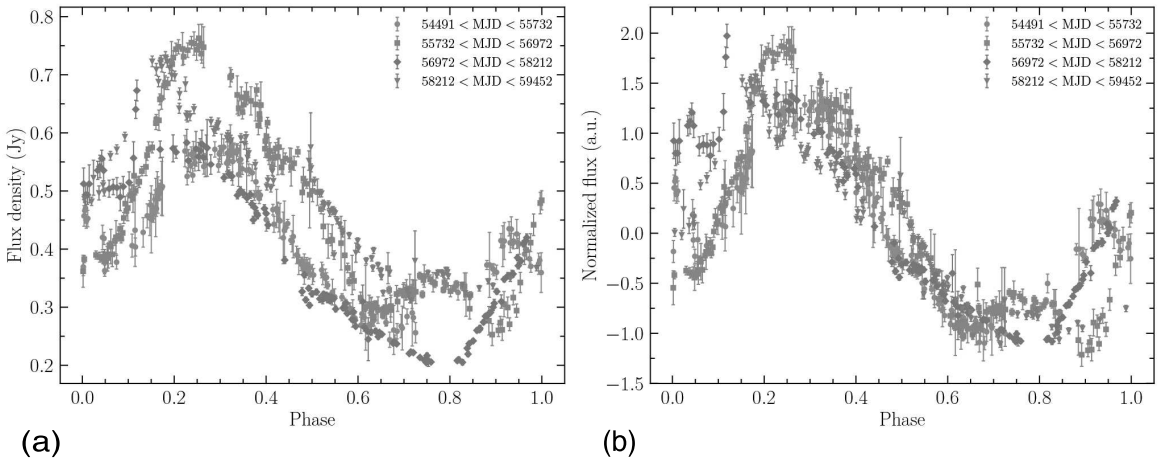

Figure 5. Light curve of PKS J0805−0111 folded with a period of 1240.7 days. Note that in the final cycle the sinusoidal variation ceases at MJD 59041, so that the final portion of the light curve diverges from the other three curves. (a) The light curves showing the observed flux densities in jansky. (b) The data in each period normalized to the same offset (0) and amplitude (1): i.e., normalized flux density = (flux density − S_0)/A.

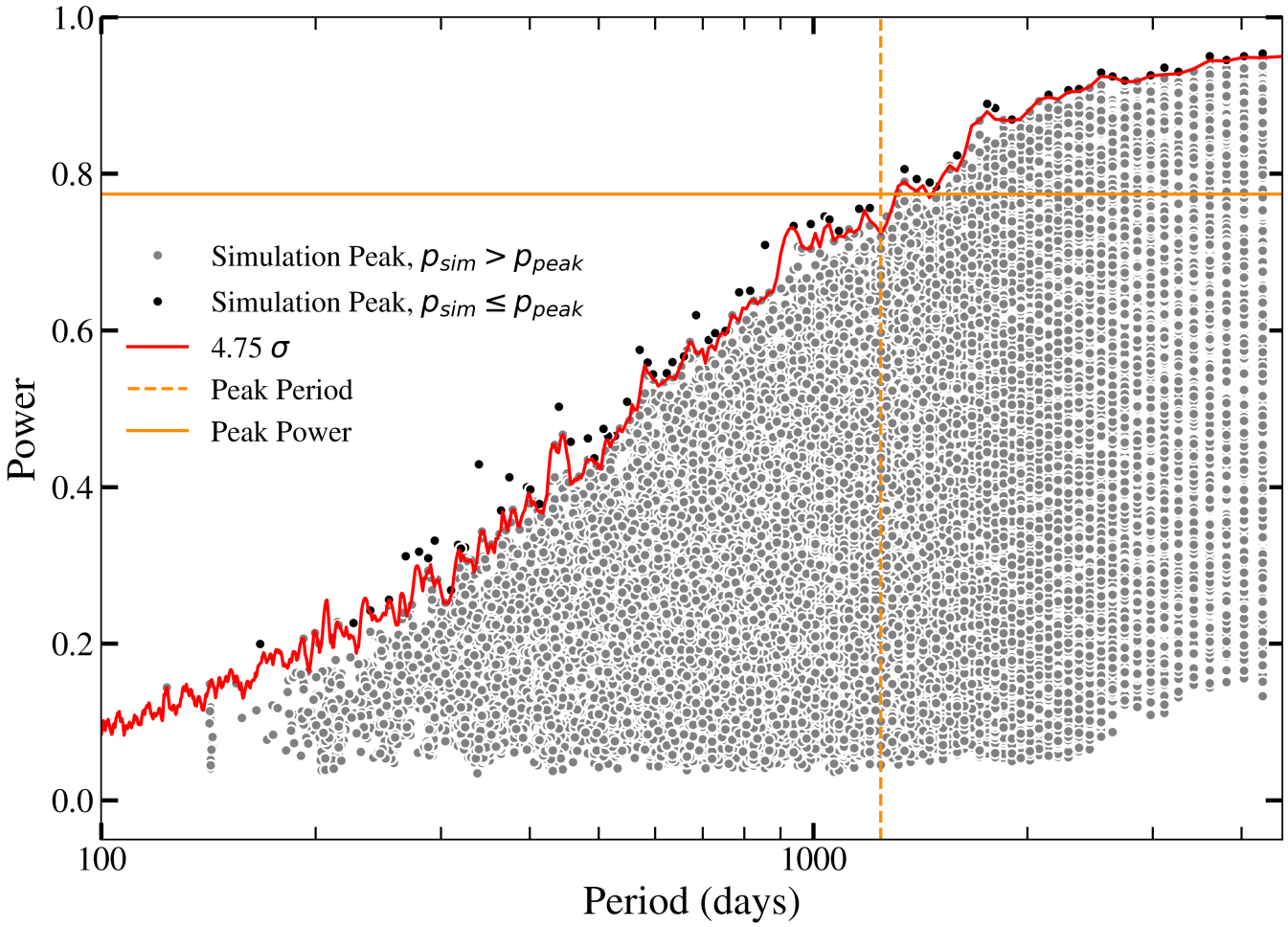

Figure 6. The generalized Lomb–Scargle peak power and period for each of the 1,000,000 simulations is shown by the circles. Simulations where the local p-value $p_{\rm sim}$ is equal to or smaller than the local p-value of the observed GLS periodogram peak $p_{\rm peak}$ are shown as black dots, whereas gray dots indicate $p_{\rm sim} > p_{\rm peak}$. The values of the period and power of the most significant peak in the GLS periodogram for PKS J0805−0111 are shown by the vertical dashed and horizontal orange lines, respectively. Note that the 4.75σ line refers to the situation where the periods are known a priori. This sigma level is given by the local p-value calculated at the observed peak, $p_{\rm peak} < 1/1{,}000{,}000$. In the absence of such knowledge one has to use the global significance, which is the fraction of black dots among all 1,000,000 dots. The global significance is considerably lower than what one would determine from the 4.75σ curve shown here (see O22). The quantization of the periods is due to the selection of the frequency resolution for the analysis, $\Delta f = 1/(\zeta T)$, with $\zeta = 15$.

Table 2
GLS Probability and Significance Level from Matched Red-noise Tail Simulations—Isolated Case

Test	GLS $\mathcal{P}_{\rm peak}$ (max. = 1)	Total simulations	Number of simulations that pass test	p-value[a]	Significance[a]
Global significance	0.77	1,000,000	67	6.7×10^{-5}	3.82σ

Note. $\mathcal{P}$ is the GLS power. We count simulations at all periods with local p-values less than the local p-value of the peak in Figure 2. The period of the peak is $P_{\rm peak} = 1245 \pm 139$ days.
[a] The significance values reported in this table do *not* take into account the observed sample size of 1158 blazars (see Section 5).

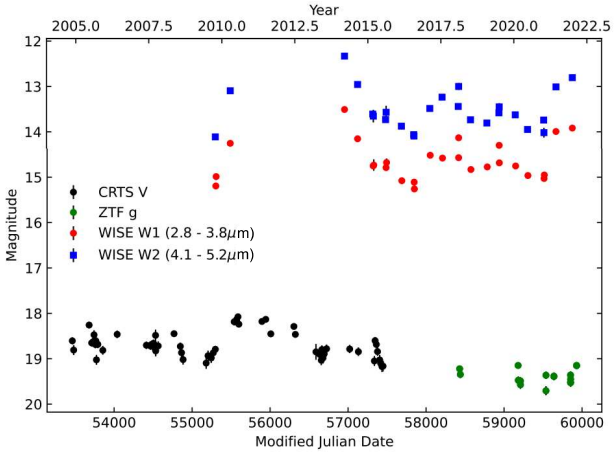

Figure 7. The archival optical and infrared light curve of PKS J0805−0111 showing data from CRTS (black circles), ZTF g (green circles), WISE W1 (red circles), and WISE W2 (blue squares).

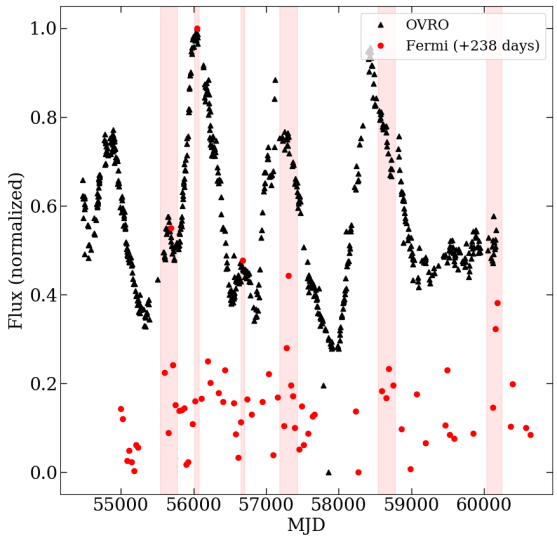

Figure 8. Normalized 15 GHz and GeV γ-ray light curves. The γ-ray light curve has been shifted forward in time by 238 days. The red shaded areas mark the periods of increased detection significance.

8 ks. The spectrum is characterized by a power law of photon index $\Gamma \simeq 2.2$, moderately absorbed by an intrinsic hydrogen column density of $8.5 \times 10^{21}\,{\rm cm}^{-2}$ in the rest frame ($z = 1.388$). The addition of an extra neutral Fe Kα line improves the fit only marginally, though the observation is rather shallow. We conclude that the X-ray spectrum of PKS J0805−011 is well described by an absorbed featureless power law. Future follow-up monitoring with large field-of-view X-ray instruments like Swift and eRosita will be promising, as simulations have predicted that close-separation accreting SMBHBs will have a periodically modulated hard X-ray component whose period is of the order of the binary orbital period (Y. Tang et al. 2018; J. H. Krolik et al. 2019).

PKS J0805−0111 is in the top 26% brightest γ-ray sources observed by the Fermi gamma-ray space telescope (S. Abdollahi et al. 2020; M. Ajello et al. 2022). It is included in the Fermi light-curve repository[21] (S. Abdollahi et al. 2023), from which we extracted the 30 days binned (0.1–100 GeV) light curve shown in Figure 8. We used the detection significance in each bin (test statistic) to identify periods of increased significance and hence higher flux. We then matched the highest flux observed in γ-rays to the highest flux density measured at 15 GHz. This requires shifting the γ-ray light curve forward in time by 238 days (MJD + 238 days). Figure 8 shows the normalized 15 GHz and γ-ray light curves shifted in time. It is evident that all the periods of increased γ-ray flux coincide roughly with peaks in the radio emission.

We interpret the shift of 238 days as an indication that the γ-ray flux originates much closer to the central engine than the 15 GHz emission.

[21] https://fermi.gsfc.nasa.gov/ssc/data/access/lat/lightcurveRepository/

8. The Tip of the Iceberg

We have detected two blazars showing strong sinusoidal variations that dominate their radio light curves among the blazars in the OVRO 40 m Telescope monitoring program. It is important to recognize that, regardless of whether these candidates are SMBHBs or not, these two examples are both exceptional in the strengths of their sinusoidal variations relative to their random flux density variations. It is almost surely the case therefore that there are many other blazars in this large sample with similar sinusoidal variations that do not dominate the light curve, and remain as yet undetected, so that the two cases we have reported represent only "the tip of the iceberg" and there must be many more such cases. If a significant fraction of these blazars exhibiting sinusoidal variations are SMBHBs, then the high rate of occurrence will pose a challenge to theories of the formation of SMBHBs in galactic nuclei.

We are engaged in a comprehensive study of the 40 m Telescope light curves in which we add sinusoidal variations to the light curves and then subject them to the GLS analysis described above in order to determine the probability of detecting the added sinusoid. These tests are complicated by the fact that the sinusoids can disappear and reappear with different amplitudes.

Another aspect of the detection of two strong SMBHB candidates out of our monitoring sample of 1158 blazars is that, if these candidates are confirmed as SMBHBs, then our two cases out of 1158 represent a lower limit to the number of

SMBHBs in the sample. In the kinetic orbit model (S. Kiehlmann et al. 2025; O22), the amplitude of the sinusoidal variability scales as $\cos i$ (O22), where i is the inclination between the orbital angular momentum axis and the line of sight, so that, for geometric reasons, we may not detect some SMBHB candidates. The standard deviation of residuals from the best-fit sine-wave model (Figure 1) is 0.068 Jy. It is unlikely that we would be able to securely detect sinusoidal variations with an amplitude smaller than this. Assuming that the observed amplitude (0.171 Jy) is close to the maximum possible, we would not be able to detect the sinusoidal variations if $|i| > \arccos(0.068/0.171) = 67°$. If the orbits were distributed randomly, we would miss $(90 - 67)/90 \sim 25\%$ of the SMBHs for simply geometric reasons. If we adopt a much more rigorous criterion for the detection of the periodicity (3σ threshold), it is quite possible that we may miss more than 50% of SMBHBs. If, in addition, we include the fact that the sinusoidal variations can appear and disappear on the timescale of one period, as seen in both PKS 2131−021 (O22) and PKS J0805−0111 (this paper), and which we think is likely due to variation in the fueling, then it is clear that we will miss most of the SMBHBs in the monitoring sample.

The first blazar in our monitoring sample to be identified as a quasi-periodic oscillator was PG 1553+113 (M. Ackermann et al. 2015), in which the quasi-periodic oscillator was discovered in the Fermi-LAT light curve. This object shows only hints of quasi-periodic oscillations in the OVRO 15 GHz light curve. The γ-ray periodicity has been confirmed (S. Abdollahi et al. 2024), and shown to pass the 3σ criterion (MAGIC Collaboration et al. 2024) that we have adopted as the threshold for strong SMBHB candidates (O22). Thus there are at least three *strong* SMBHB candidates in the complete statistical sample of 1158 blazars defined by J. L. Richards et al. (2011). This places a lower limit on the fraction of blazars that are SMBHBs of $\sim$1 in 400.

For these reasons, we estimate that the fraction of SMBHB candidates among blazars could be as high as $\sim$1 in 100.

9. Gravitational-wave Emission

If PKS J0805−0111 is indeed a binary of supermassive black holes, it will produce gravitational waves with Earth-frame frequency $f_{\mathrm{GW}\oplus} = 2/P_{\oplus} \simeq 18.7$ nHz, within the sensitive range of pulsar timing arrays such as NANOGrav (G. Agazie et al. 2023a), where $P_{\oplus}$ is the period that we observe in the light curve. For a quasi-circular orbit, the gravitational-wave strain is given by (M. Maggiore 2008)

$$h_{\mathrm{GW}} = \frac{2(G\mathcal{M}_{\oplus})^{5/3}(\pi f_{\mathrm{GW}\oplus})^{2/3}}{c^4 D_L}, \quad (4)$$

where $D_L \simeq 10$ Gpc is the luminosity distance and $\mathcal{M}_{\oplus} = (1+z) \times (M_1 M_2)^{3/5}/(M_1 + M_2)^{1/5}$ is the Earth-frame chirp mass, here given as a function of the rest-frame component masses $M_{1,2}$ and the redshift $z = 1.388$ (S. E. Healey et al. 2008).

By means of Equation (4), the upper limits on h_{GW} induce limits on the mass of the putative binary. Specifically, taking the all-sky limit at $f_{\mathrm{GW}\oplus}$ derived from the 15 yr NANOGrav data set (G. Agazie et al. 2023b) and calibrating it to the sky location of PKS J0805−0111 by way of the 6 nHz sky map (G. Agazie et al. 2023b) yields a 95% Bayesian upper limit $h_{\mathrm{GW}} \lesssim 10^{-14}$. Under the assumption that the binary is approximately face-on, this translates to a rest-frame chirp mass $\mathcal{M} \lesssim 5 \times 10^9\, M_{\odot}$, or to a limit $M \lesssim 11.4 \times 10^9\, M_{\odot}$ for the total rest-frame mass in a symmetric-mass binary. A joint constraint using electromagnetic data, as performed by Z. Arzoumanian et al. (2020) for 3C 66B, could improve on these limits by a factor of $\sim$2.

As long as $\mathcal{M} \gtrsim 10^9\, M_{\odot}$, the binary would be detectable with future pulsar timing arrays that include pulsars identified by the Square Kilometre Array (C. Xin et al. 2021). However, as for PKS 2131−021, such high chirp masses imply short evolution times to binary coalescence ($\sim$2000 yr $\times$ $(\mathcal{M}/10^9\, M_{\odot})^{-5/3}$), casting doubt on the plausibility of observing such a massive late-stage system (O22).

10. Conclusion

Given that PKS J0805−0111 exhibits five of the likely characteristics of SMBHBs in blazars that we found in PKS 2131−021, and the $\sim$0.003 probability of finding two such cases of red-noise-induced periodicity in our sample of 1158 objects, the evidence shows that PKS J0805−0111 should certainly be regarded as a strong SMBHB candidate.

The fact that the sinusoidal variations in PKS J0805−0111 have now disappeared, in a manner very similar to the disappearance of the sinusoidal variations in PKS 2131−021 in 1984, suggests a prediction based on the PKS 2131−021 behavior: namely, that the sinusoidal variations will reappear in PKS J0805−0111 after a gap of some years (in PKS 2131−021 the gap was 19 yr), with the same period and in phase with the sinusoidal variations we are reporting here. In addition, continued monitoring of all of the sources in the sample, including those that have hitherto shown no sign of periodicity, is very well-motivated. If and when more transitions are seen, multiwavelength monitoring is also well-motivated.

We have now identified two blazars, PKS J0805−0111 and PKS 2131−021, that show strong sinusoidal variations having a global significance p-value $< 1.3 \times 10^{-3}$, i.e., $> 3\sigma$, which we interpret as real, and not due to random variations caused by the red-noise tail in the PSD. The detection of a second strong SMBHB candidate showing sinusoidal variations demonstrates that PKS 2131−021 is not an isolated case. Indeed, since we have picked out only blazars for which the light curves are dominated by the sinusoidal signal for most of the observing period of the 40 m Telescope, which must be the objects in our sample with orbits that are close to face-on, there must be several candidates at significantly more oblique angles for every face-on candidate we find. Thus it is clear that $\sim$1 in 100 bright radio blazars must be SMBHB candidates, which has interesting implications for searches for the SMBHB signal with pulsar timing arrays.

As argued by S. Kiehlmann et al. (2025) for the case of PKS 2131−021, a good approach to improving our understanding of SMBHB candidates is to perform high-sensitivity and high-resolution ($R \sim 5000$–$10{,}000$) optical and near-infrared spectroscopy. It would be surprising if the various dynamical explanations that have been advanced to account for the observed coherent variation in the flux density in several bands did not also produce some spectroscopic variation. It is not necessary to observe for the entire 3.4 yr period: systematic changes over a month or so may well be detectable and interpretable kinematically if seen, and would motivate longer-term monitoring.

Acknowledgments

This work is supported by NSF grants AST2407603 and AST2407604. We thank the California Institute of Technology and the Max Planck Institute for Radio Astronomy for supporting the OVRO 40 m program under extremely difficult circumstances over the last eight years in the absence of agency funding. Without this private support this paper would not have been written. We also thank all the volunteers who have enabled this work to be carried out. Prior to 2016, the OVRO program was supported by NASA grants NNG06GG1G, NNX08AW31G, NNX11A043G, and NNX13AQ89G from 2006 to 2016 and NSF grants AST-0808050, and AST-1109911 from 2008 to 2014. The UMRAO program received support from NSF grants AST-8021250, AST-8301234, AST-8501093, AST-8815678, AST-9120224, AST-9421979, AST-9900723, AST-0307629, AST-0607523, and earlier NSF awards, and from NASA grants NNX09AU16G, NNX10AP16G, NNX11AO13G, and NNX13AP18G. Additional funding for the operation of UMRAO was provided by the University of Michigan. The NANOGrav project receives support from National Science Foundation (NSF) Physics Frontier Center award number 1430284. T.H. was supported by the Academy of Finland projects 317383, 320085, 322535, and 345899. S.K. and K.T. acknowledge support from the European Research Council (ERC) under the European Union's Horizon 2.20 research and innovation program under grant agreement No. 771282. I.L. and S.K. were funded by the European Union ERC-2022-STG —BOOTES—101076343. Views and opinions expressed are however those of the author(s) only and do not necessarily reflect those of the European Union or the European Research Council Executive Agency. Neither the European Union nor the granting authority can be held responsible for them. W.M. acknowledges support by the ANID BASAL project FB210003 and FONDECYT 11190853. R.R. and B.M. and P.V.d.l.P. acknowledge support from ANID Basal AFB-170002, from Núcleo Milenio TITANs (NCN2023_002), and CATA BASAL FB210003. P.V.d.l.P. also acknowledges support by the National Agency for Research and Development (ANID)/Scholarship Program/Doctorado Nacional/2023–21232103. M.V. performed part of this work at the Jet Propulsion Laboratory, California Institute of Technology, under a contract with the National Aeronautics and Space Administration (80NM0018D0004). V.P. acknowledges support from the Foundation of Research and Technology—Hellas Synergy Grants Program through project MagMASim, jointly implemented by the Institute of Astrophysics and the Institute of Applied and Computational Mathematics and by the Hellenic Foundation for Research and Innovation (H.F.R.I.) under the "First Call for H.F.R.I. Research Projects to support Faculty members and Researchers and the procurement of high-cost research equipment grant" (Project 1552 CIRCE). K.T. acknowledges support from the Foundation of Research and Technology—Hellas Synergy Grants Program through project POLAR, jointly implemented by the Institute of Astrophysics and the Institute of Computer Science. I.L. was supported by the NASA Postdoctoral Program at the Marshall Space Flight Center, administered by Oak Ridge Associated Universities under contract with NASA. The authors acknowledge the Kultrun Astronomy Hybrid Cluster (projects Conicyt Programa de Astronomia FondoQuimal QUIMAL170001, QUIMAL220002 and Conicyt PIA ACT172033) for providing HPC resources that have contributed to the research results reported in this paper.

Appendix A
Simulations and Significance

For this study, we simulated light curves that best match the PSD, the PDF, sampling, and observational noise of the observed light curve under the assumption of a power-law red-noise process. Specifically, we assumed that the PSD $=\text{constant}\times\nu^{-\beta}+P_{\text{white}}$, where ν is the frequency. We followed a procedure based on P. Uttley et al. (2002) and W. Max-Moerbeck et al. (2014) to obtain the slope that best matches the observed PSD, in the case of PKS J0805−0111 $\beta=1.85$ [1.75–2.083], see Figure 9. The simulated light curves, which at this step are 10 times longer than the observed light curve and have 10 times higher cadence, were then resampled to match the original sampling pattern.

A noise floor level P_{white} was added to account for the flux density uncertainties. To calculate the contribution of P_{white} we assumed white noise $\mathcal{N}(0, \sigma_e^2)$ where σ_e^2 is the mean variance of the uncertainties. Then, using Parseval's theorem, we estimate the contribution of P_{white}:

$$\sigma_e^2 = \int_{\nu_0}^{\nu_1} P(\nu)d\nu = P_{\text{white}} \int_{\nu_0}^{\nu_1} d\nu = P_{\text{white}}(\nu_1 - \nu_0),$$

where ν_0 is the lowest sampled frequency, f_{low}, and ν_1 is the highest sampled frequency, f_{high}.

Note that the second and third points of the observed PSD in Figure 9 deviate from a general linear trend. This increased power over the typical power-law red-noise spectrum at these frequencies is the contribution of the periodic signal. The simulations implement the pure red-noise hypothesis and therefore do not systematically reproduce this peak.

Considering the non-Gaussian PDF (see Figure 10) we adopted the algorithm introduced by D. Emmanoulopoulos et al. (2013) for our simulations. This algorithm allows us to create simulations with the above PSD and a PDF matching that of the observed light curve. For characterizing the PDF we used the empirical cumulative distribution function. Due to the cyclic nature of the fast Fourier transform, we are extending the light curves generated by 30%, and then cropping the edges to avoid edge effects. The purpose is to avoid spurious

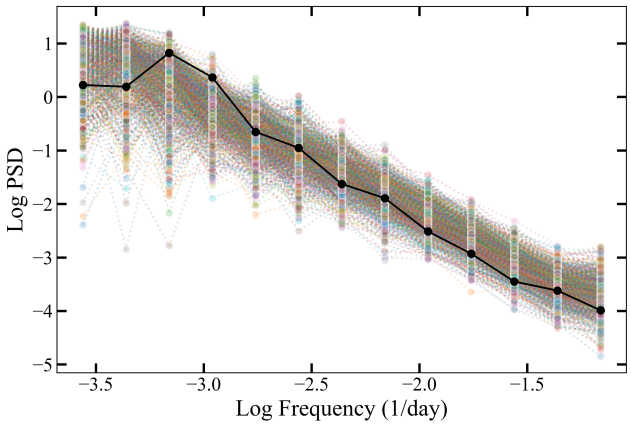

Figure 9. Power spectral density over frequency. Black dots and line: the observed PSD of PKS J0805−0111. Colored dots and lines: PSDs of 1000 randomly selected simulations.

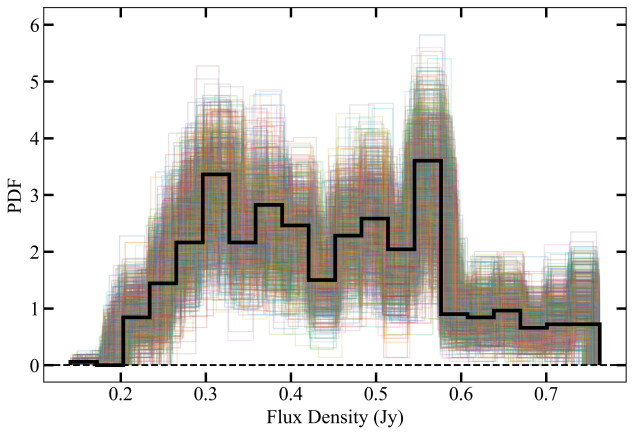

Figure 10. Probability density function. Black histogram: the observed PDF of PKS J0805−0111. Colored dots and lines: PDFs of 1000 randomly selected simulations.

correlations between the first and last data points in the simulations. By extending the curve length, we minimize these edge effects, ensuring a more accurate representation of the original signal without significantly sacrificing performance or convergence. The PDF of the simulations matches the observed PDF, see Figure 10.

After generating the artificial light curves, we carried out a rigorous significance analysis of periodicity detections through the following steps:

1. We calculated the power spectra of observed data and simulated light curves using the GLS periodogram. For this study, the number of simulations is 1,000,000.
2. We compared the strongest observed peak, at its specific period, with the ensemble of simulated GLS periodograms. Specifically, we counted the fraction of simulations where the GLS power is equal to or greater than the observed peak at the same period. This gives us the *local* p-value $p_{\rm peak}$, i.e., evaluated at the peak period. To account for the *look-elsewhere effect* (O22) of analyzing a large number of frequencies we carried out two additional steps.
3. In the same fashion as for the observed data, we identified the strongest peak in the GLS periodogram of each simulation and calculated its local p-value.
4. Finally, we counted the fraction of simulations for which the local p-value $p_{\rm sim}$ is equal to or lower than the observed local p-value. This gave us the *global* p-value.

The local p-value can only be used if the period is known a priori from independent tests. If that is not the case, as in this case, we have to use the global p-value. We use a conservative threshold of p-value $<1.3\times10^{-3}$, equivalent to a significance level $>3\sigma$, to reject the hypothesis that the periodic signal arises spuriously from a red-noise process.

Appendix B
Subtracted Sine Wave

The significance analysis we described above is based on the hypothesis that the radio light curve of PKS J0805−0111 follows a red-noise process with a power-law PSD with power-law index $\beta=1.85$ [1.75–2.083] estimated from the spectrum shown in Figure 9, which gives us the best-matching purely stochastic model of the light curve. We rejected this model with a global p-value of 6.7×10^{-5} at the 3.82σ significance level. However, Figure 9 shows that the periodic signal is visible in the PSD as increased power at the third and fourth lowest tested frequencies. This may bias our estimation of power-law index toward steeper spectra.

In order to verify that a possible bias in the estimation of PSD index does not affect our conclusion, we carried out a second analysis using the residual light curve after subtracting the sinusoidal component. The black curve in Figure 1 shows the residual light curve. From these data we estimated a PSD power-law index $\beta=1.6$ [1.5–1.7], corresponding to a flatter PSD than estimated from the original data. We repeated the entire periodicity analysis with simulations that have $\beta=1.6$ and found a global p-value of 7.8×10^{-5}, which differs by only a factor of 1.16 from our first result and therefore has no effect on our findings. We conclude that our results do not depend on the specific PSD slope value and are not affected by any potential bias that a spurious or intrinsic period may introduce into the PSD estimate.

Appendix C
Convergence of the Global p-value

It is important to estimate the accuracy of the global p-value, which depends on the total number of simulations. We methodically generated different subsets from our 1,000,000 simulations. From each subset we calculated the global p-value. We need to distinguish two situations that depend on the local p-value:

1. *Case I: local p-value >0.* Figure 11 shows how the global p-value and its accuracy depend on the number of simulations, based on the OVRO 40 m data of PKS J0805−0111 with sine wave subtracted, where the residuals generate a peak at a period of 2445 days with a local p-value of $\sim1.89\times10^{-2}$ and a global p-value of $\sim1.8\times10^{-1}$. When the local p-value is well defined, increasing the number of simulations reduces the scatter of the estimated global p-value around the true value. The larger scatter at fewer simulations arises from the stochastic nature of the simulations. The reduction in the scatter indicates that we reached adequate accuracy with

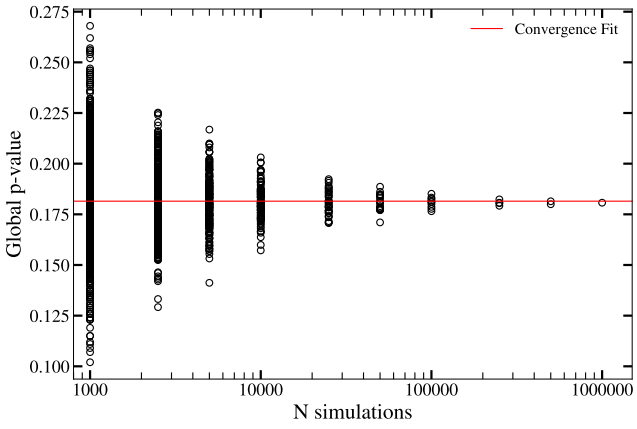

Figure 11. Convergence of global p-value with increasing number of simulations when the local p-value is >0. Based on the OVRO 40 m and the strongest peak in residual GLS data of PKS J0805−0111 with sine wave subtracted.

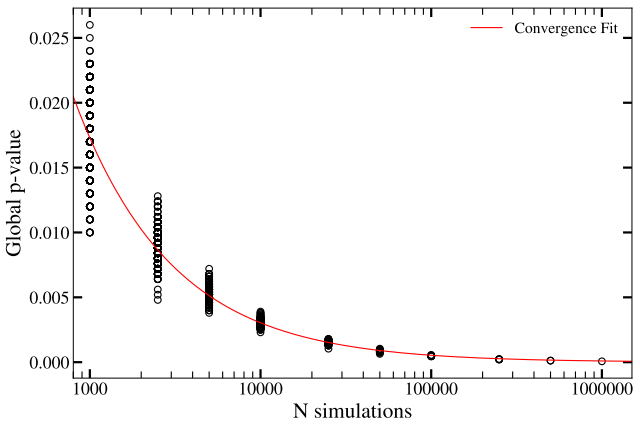

Figure 12. Convergence of global p-value with increasing number of simulations when the local p-value is 0. Based on the OVRO 40 m and the strongest peak in GLS data of PKS J0805−0111.

1,000,000 simulations in this particular case; the behavior of the convergence can be seen in Figure 11.

2. *Case II: local* p*-value equal to 0.* Figure 11 shows how the global p-value and its accuracy depend on the number of simulations, based on the OVRO 40 m data of PKS J0805−0111 as discussed in this paper. A local p-value equal to 0 means that none of our 1,000,000 simulations have a GLS periodogram power at least as strong as the power of the GLS periodogram of the observed light curve at the peak period, $P_{\rm peak}$. Therefore, the local p-value is not well estimated, but rather has an upper limit of $<1/1{,}000{,}000$. Accordingly, a smaller subset of simulations results in a higher upper limit on the local p-value, which then results in a higher upper limit on the global p-value. Consequently, the estimate of the global p-value decreases with increasing number of simulations and converges toward the true value. In this case the global p-value is biased toward being overestimated and rather poses an upper limit. Similar to case I, increasing the number of simulations also reduces the scatter in the estimate of the p-value, or more accurately its upper limit. In the case of PKS J0805−0111, Figure 12 indicates that we have reached adequate accuracy in the estimate of the p-value and we have passed our 3σ-confidence limit with 1,000,000 simulations. Whereas further increasing the number of simulations would give us a more accurate estimate of the p-value, it would not change our conclusions.

ORCID iDs

P. V. de la Parra https://orcid.org/0000-0001-5957-1412
S. Kiehlmann https://orcid.org/0000-0001-6314-9177
P. Mróz https://orcid.org/0000-0001-7016-1692
A. C. S. Readhead https://orcid.org/0000-0001-9152-961X
M. C. Begelman https://orcid.org/0000-0003-0936-8488
R. D. Blandford https://orcid.org/0000-0002-1854-5506
Y. Ding https://orcid.org/0000-0002-5770-2666
F. Harrison https://orcid.org/0000-0002-4226-8959
I. Liodakis https://orcid.org/0000-0001-9200-4006
W. Max-Moerbeck https://orcid.org/0000-0002-5491-5244
R. Reeves https://orcid.org/0000-0001-5704-271X
M. Vallisneri https://orcid.org/0000-0002-4162-0033
M. F. Aller https://orcid.org/0000-0003-2483-2103
M. J. Graham https://orcid.org/0000-0002-3168-0139
T. Hovatta https://orcid.org/0000-0002-2024-8199
A. A. Mahabal https://orcid.org/0000-0003-2242-0244
T. J. Pearson https://orcid.org/0000-0001-5213-6231
V. Ravi https://orcid.org/0000-0002-7252-5485
K. Tassis https://orcid.org/0000-0002-8831-2038
J. A. Zensus https://orcid.org/0000-0001-7470-3321

References

Abdollahi, S., Acero, F., Ackermann, M., et al. 2020, ApJS, 247, 33
Abdollahi, S., Ajello, M., Baldini, L., et al. 2023, ApJS, 265, 31
Abdollahi, S., Baldini, L., Barbiellini, G., et al. 2024, ApJ, 976, 203
Ackermann, M., Ajello, M., Albert, A., et al. 2015, ApJL, 813, L41
Agazie, G., Anumarlapudi, A., Archibald, A. M., et al. 2023a, ApJL, 951, L8
Agazie, G., Anumarlapudi, A., Archibald, A. M., et al. 2023b, ApJL, 951, L50
Ajello, M., Baldini, L., Ballet, J., et al. 2022, ApJS, 263, 24
Aniello, T., Antonelli, L. A., Tombesi, F., et al. 2024, A&A, 686, A300
Arcodia, R., Merloni, A., Nandra, K., et al. 2021, Natur, 592, 704
Arzoumanian, Z., Baker, P. T., Brazier, A., et al. 2020, ApJ, 900, 102
Begelman, M. C., Blandford, R. D., & Rees, M. J. 1980, Natur, 287, 307
Bhatta, G., Mohorian, M., & Bilinsky, I. 2018, A&A, 619, A93
Charisi, M., Bartos, I., Haiman, Z., et al. 2016, MNRAS, 463, 2145
Chen, Y., Yi, T., Chen, J., et al. 2024, NewA, 108, 102186
Ciaramella, A., Bongardo, C., Aller, H. D., et al. 2004, A&A, 419, 485
Conselice, C. J. 2014, ARA&A, 52, 291
Dermer, C. D., & Schlickeiser, R. 1993, ApJ, 416, 458
Dey, L., Valtonen, M. J., Gopakumar, A., et al. 2021, MNRAS, 503, 4400
D'Orazio, D. J., & Charisi, M. 2023, arXiv:2310.16896
Drake, A. J., Djorgovski, S. G., Mahabal, A., et al. 2009, ApJ, 696, 870
Emmanoulopoulos, D., McHardy, I. M., & Papadakis, I. E. 2013, MNRAS, 433, 907
Emmanoulopoulos, D., McHardy, I. M., & Uttley, P. 2010, MNRAS, 404, 931
EPTA CollaborationInPTA Collaboration, Antoniadis, J., et al. 2023, A&A, 678, A50
Foreman-Mackey, D., Hogg, D. W., Lang, D., & Goodman, J. 2013, PASP, 125, 306
Foster, G. 1996, AJ, 112, 1709
Franchini, A., Bonetti, M., Lupi, A., et al. 2023, A&A, 675, A100
Graham, M. J., Djorgovski, S. G., Stern, D., et al. 2015, Natur, 518, 74
Graham, M. J., Kulkarni, S. R., Bellm, E. C., et al. 2019, PASP, 131, 078001
Gupta, A. C., Tripathi, A., Wiita, P. J., et al. 2018, A&A, 616, L6
Healey, S. E., Romani, R. W., Cotter, G., et al. 2008, ApJS, 175, 97
Healey, S. E., Romani, R. W., Taylor, G. B., et al. 2007, ApJS, 171, 61
Hopkins, P. F., Hernquist, L., Cox, T. J., & Kereš, D. 2008, ApJS, 175, 356
Kiehlmann, S., De La Parra, P. V, Sullivan, A., et al. 2025, ApJ, 985, 59
Komatsu, E., Dunkley, J., Nolta, M. R., et al. 2009, ApJS, 180, 330
Krolik, J. H., Volonteri, M., Dubois, Y., & Devriendt, J. 2019, ApJ, 879, 110
Maggiore, M. 2008, Gravitational Waves: Vol. 1: Theory and Experiments (Oxford: Oxford Univ. Press)
MAGIC Collaboration, Abe, H., Abe, S., et al. 2024, MNRAS, 529, 3894
Masci, F. J., Laher, R. R., Rusholme, B., et al. 2019, PASP, 131, 018003
Mastichiadis, A., & Kirk, J. G. 2002, PASA, 19, 138
Max-Moerbeck, W., Richards, J. L., Hovatta, T., et al. 2014, MNRAS, 445, 437
Medd, W. J., Andrew, B. H., Harvey, G. A., & Locke, J. L. 1972, MmRAS, 77, 109
Miniutti, G., Saxton, R. D., Giustini, M., et al. 2019, Natur, 573, 381
O'Neill, S., Kiehlmann, S., Readhead, A. C. S., et al. 2022, ApJL, 926, L35
Planck Collaboration, Aghanim, N., Akrami, Y., et al. 2020, A&A, 641, A6
Ragazzini, J. R., & Zadeh, L. A. 1952, Transactions of the American Institute of Electrical Engineers, Part II: Applications and Industry, 71, 225
Readhead, A. C. S., Lawrence, C. R., Myers, S. T., et al. 1989, ApJ, 346, 566
Ren, G.-W., Ding, N., Zhang, X., et al. 2021a, MNRAS, 506, 3791
Ren, G.-W., Zhang, H.-J., Zhang, X., et al. 2021b, RAA, 21, 075
Richards, J. L., Max-Moerbeck, W., Pavlidou, V., et al. 2011, ApJS, 194, 29
Sikora, M. 1994, ApJS, 90, 923
Sillanpaa, A., Haarala, S., Valtonen, M. J., Sundelius, B., & Byrd, G. G. 1988, ApJ, 325, 628
Tang, Y., Haiman, Z., & MacFadyen, A. 2018, MNRAS, 476, 2249
Timmer, J., & Koenig, M. 1995, A&A, 300, 707
Uttley, P., McHardy, I. M., & Papadakis, I. E. 2002, MNRAS, 332, 231
Valtonen, M. J., Zola, S., Ciprini, S., et al. 2016, ApJL, 819, L37
Wang, Y., Wang, T., Ho, L. C., Zhong, Y., & Luo, B. 2024, A&A, 689, A327
Welsh, W. F. 1999, PASP, 111, 1347
Xin, C., Mingarelli, C. M. F., & Hazboun, J. S. 2021, ApJ, 915, 97
Zechmeister, M., & Kürster, M. 2009, A&A, 496, 577